Microporous and Mesoporous Materials 392 (2025) 113621

Contents lists available at ScienceDirect

Microporous and Mesoporous Materials

journal homepage: www.elsevier.com/locate/micromeso

3D-printed activated carbon monoliths for efficient CO_2 capture

Henrry Ortega-Ortiz [a,b], Laura M. Esteves [c], Andreia F.M. Santos [a], Jeniffer Carrillo [b,d], Isabel M. Fonseca [a], José P.B. Mota [a], Inês Matos [a,**], Rui P.P.L. Ribeiro [a,e,*]

[a] LAQV-REQUIMTE, Department of Chemistry, NOVA School of Science and Technology, NOVA University of Lisbon, 2829-516, Caparica, Portugal
[b] Chemical Engineering Group, Engineering and Architecture Faculty, Universidad de Pamplona, 543050, Pamplona, Colombia
[c] Centro de Química Estrutural (CQE), Institute of Molecular Sciences (IMS), Instituto Superior Técnico, University of Lisbon, Av. Rovisco Pais, 1049-001, Lisbon, Portugal
[d] GISM Group, Engineering and Architecture Faculty, Universidad de Pamplona, 543050, Pamplona, Colombia
[e] HyLab – Green Hydrogen Collaborative Laboratory, Estrada Nacional 120-1, Central Termoeléctrica, 7520-089, Sines, Portugal

ARTICLE INFO

Keywords:
Adsorption
Activated carbons
Structured adsorbent
3D-printing
Fused deposition modeling
CO_2 capture

ABSTRACT

In gas-phase adsorption processes, adsorbents are typically used as beads or pellets in a fixed bed. While these shapes permit their application in adsorption processes, they fall short of achieving optimal performance. This limitation can be greatly improved by employing structured materials, which offer reduced pressure drop and enhanced mass and energy transfer, thereby improving the overall process efficiency. Herein, resol-based activated carbons (ACs) are structured using 3D-printed sacrificial water-soluble templates to produce custom-designed monoliths for efficient carbon dioxide (CO_2) capture. The influence of activation conditions (time under CO_2 flow) on textural properties, CO_2 adsorption capacity, and CO_2/nitrogen (N_2) selectivity are investigated. Prolonging the activation time leads to a progressive increase in surface area and micropore volume, as more carbon is removed through gasification reactions with CO_2. The resulting enhancement in porosity improves the CO_2 adsorption capacity. However, the AC with the lowest burn-off has the highest selectivity for CO_2 over N_2 (considering a binary CO_2/N_2 mixture with 15 mol% of CO_2) due to its lower ability to adsorb N_2. Overall, this work highlights the potential of a modern 3D-printing fused deposition modeling technique to engineer structured adsorbents with applications in gas separation processes, such as CO_2 capture.

1. Introduction

It is known that greenhouse gases (GHGs) play a crucial role in regulating the planet's temperature. The rapid increase in GHG emissions, particularly carbon dioxide (CO_2), has led to significant environmental concerns [1,2], contributing to global warming and its associated impacts, such as rising sea levels, extreme weather events, and ecosystem disruptions [1,3]. As a result, addressing CO_2 emissions has become a critical focus of environmental policy and scientific research. To mitigate the effects of increased CO_2 emissions, multiple Carbon Capture and Storage (CCS) and Carbon Capture and Utilization (CCU) technologies have been developed [4,5]. The latter provides an alternative approach by converting captured CO_2 into value-added products, including chemicals, fuels, and materials [6]. Among the CCS/CCU approaches, post-combustion capture offers the advantage of flexibility, enabling capture systems to be retrofitted into existing infrastructure with minimal modifications. This is particularly important, as many power plants and industrial facilities are relatively new and expected to remain operational for decades [2,7]. Given these considerations, developing sustainable and economically feasible technological solutions to overcome this challenge is essential.

A widely used method for capturing CO_2 is adsorption. This approach takes advantage of the high specific surface area and large micropore volume of solid adsorbents, such as zeolites, metal-organic frameworks (MOFs), and activated carbons (ACs), to separate CO_2 from gas mixtures, being also a simple technique with low energy consumption and no liquid waste. While zeolites are promising due to their high adsorption capacities and fast kinetics, their performance is limited by poor moisture tolerance and high regeneration energy requirements [8–10]. Similarly, MOFs have been explored for their high specific surface area

* Corresponding author. LAQV-REQUIMTE, Department of Chemistry, NOVA School of Science and Technology, NOVA University of Lisbon, 2829-516, Caparica, Portugal.
** Corresponding author.
E-mail addresses: ines.matos@fct.unl.pt (I. Matos), rpp.ribeiro@fct.unl.pt (R.P.P.L. Ribeiro).

https://doi.org/10.1016/j.micromeso.2025.113621
Received 3 January 2025; Received in revised form 15 March 2025; Accepted 31 March 2025
Available online 2 April 2025

and tunable pore size, but they face challenges, including high synthesis cost with potentially toxic solvents, sensitivity to moisture, and vulnerability to temperature changes, being, many of them, restricted to laboratory-scale projects [2,11–13]. In contrast, ACs provide a more economically viable solution due to the abundance of carbon-based raw materials [14,15]. These structured materials are particularly attractive because of their high specific surface area and pore volume, which are critical for effective adsorption processes [2,3,5,14,16]. Moreover, the chemical versatility of ACs, which, depending on their precursors and post-treatments, can exhibit either acidic or basic characteristics that further enhance their utility as adsorbents [14,17,18]. Even though ACs generally exhibit lower adsorption capacities than zeolites at low CO_2 pressures, they are easier to regenerate, requiring less energy for desorption [19,20].

ACs are commercially available in different forms, ranging from powders to pellets and honeycomb monoliths. Powders generate high pressure drops in packed-bed systems during operation, whereas pellets, although superior in this respect, are limited in terms of mass transfer efficiency [21,22]. On the other hand, honeycomb monoliths offer significant advantages for adsorption processes, minimizing pressure drop and the risk of attrition and particle fragmentation during operation, while potentially improving flow characteristics, along with mass and energy transfer [23]. To prepare those monoliths, extrusion is one of the most common methods. However, it faces limitations regarding the ability to control the material's final shape, as any design modification requires costly and time-consuming retooling [24,25]. In contrast, 3D printing enables the creation of complex geometries without significant additional costs or effort, facilitating the development of optimized adsorbers [26] and allowing the possibility to design interconnected channels [24,25,27,28]. Therefore, this 3D printing technology emerges as an alternative to produce such materials, addressing several drawbacks inherent to the traditional extrusion methods. Additionally, 3D printing techniques are scalable and typically make an efficient use of the precursor materials, making it also cost-effective.

In fact, several structured adsorbents have been engineered with different 3D-printing technologies. Earlier studies [29,30] reported the fabrication of 3D-printed zeolite monoliths for CO_2 capture, particularly 13X, 5A [29] and ZSM-5 [30], through direct ink writing (DIW). Moreover, self-supporting gyroidal 3D-printed monoliths with zeolite 13X were prepared via digital light processing [31]. Regarding MOFs, 3D-printed MOF-74(Ni) and UTSA-16(Co) have also been produced by DIW, disclosing promising CO_2 adsorption capacities [28]. Additionally, MOF-74 and HKUST-1 were printed with capacities proportional to the MOF loading [32]. Concerning AC monoliths, 3D-printed materials prepared by stereolithography (SLA) were investigated for the impact of activation conditions on CO_2 adsorption and selectivity over N_2, revealing that variations in burn-off levels can enhance either adsorption capacity or selectivity [33]. It is known that this technique can be used to create a polymer template with specific cavities, which are subsequently filled with a precursor material that is carbonized and activated. The resulting structures showed highly controlled porosity and macrochannels [34]. Finally, examples of hybrid materials prepared by DIW with ACs have also been published. Recent studies demonstrated the effectiveness of integrating AC with zeolite 13X, originating adsorbents with high CO_2 adsorption capacities, well-formed porous networks, and excellent mechanical properties [24,25].

In this work, we present a novel method for designing AC structures based on a phenolic resin, using 3D-printed templates fabricated through the fused deposition modeling (FDM) technique. In contrast to the approaches that rely on DIW, where the required binders can compromise adsorption performance, or SLA, which involves optimizing resin photopolymerization, our methodology employs water-soluble templates to create structures composed entirely of adsorbent material. This eliminates the need for binders and allows for template removal under mild conditions using only water, avoiding toxic solvents or extreme processing conditions (e.g., high temperatures). The resulting structures were characterized to evaluate their textural, morphological, and thermal properties, as well as their adsorption capacities for CO_2 and N_2. To the best of our knowledge, this is the first study reporting the use of water-soluble templates for the fabrication of structured adsorbent materials.

2. Materials and methods

2.1. Materials

A phenolic resin, specifically referred to as resol, was used as the AC precursor. The resol synthesis used formaldehyde (CH_2O) at 37 % stabilized with methanol (VWR Chemicals), phenol (C_6H_5OH) (Thermo Scientific), sodium hydroxide (NaOH) (Laborspirit, Lda), and hydrochloric acid (HCl) at 37 % (Sigma Aldrich).

All gases were supplied by Praxair (Portugal): nitrogen (N_2, 99.99 % purity), carbon dioxide (CO_2, 99.998 % purity) and helium (He, 99.999 %).

2.2. Design and printing of the 3D template

Before the 3D printing, the geometric model of the structure was designed using the 3D CAD software Autodesk Inventor Professional 2024. An STL (Standard Tessellation Language) file of the geometric model was generated and then converted into a G-code file using the 3D printer software Repetier-Host.

The designing process began with a 3D model representing the desired AC structure. This model consisted of a tetragonal cubic monolith with straight channels aligned along the X, Y, and Z axes, as shown in Fig. 1a and b. The model was designed with wall and channel thicknesses of 2 mm, a side length of 14 mm, and a height of 26 mm. Notably, this shape cannot be produced using traditional extrusion techniques. Subsequently, the negative image of this structure was created with additional walls incorporated into the template to contain the precursor material that would fill the template once printed (see Fig. 1c).

The designed templates were 3D printed using a commercial Felix Tec 4 (Felix Printers, The Netherlands) FDM printer with a 1.75 mm diameter polyvinyl alcohol (PVA) filament (Mitsubishi Chemicals Performance Polymers). The printing parameters, including speed (20 mm/s), infill density (25 %), and extrusion temperature (483 K), were controlled via the Repetier-Host software.

2.3. Activated carbon 3D structures preparation

A procedure for preparing a low molecular weight polymer using a basic polymerization route was followed [35]. This method is based on a homogeneous catalytic reaction between phenol and formaldehyde, catalyzed by sodium hydroxide (NaOH), conducted at a molar ratio of 1:2:0.1. Phenol was added to a flask, followed by the incorporation of NaOH dissolved in deionized water. This step was performed under agitation, and once the phenol crystals had dissolved, formaldehyde was added dropwise. The mixture was stirred for 1 h at room temperature to ensure homogenization of the reactants. It was then heated to 348 K and stirred for an additional 1 h and 30 min to complete the reaction phase and facilitate monomer formation. After cooling, the pH was adjusted to 7.0 using a 1 M HCl solution. Finally, water was removed through vacuum evaporation at 318 K.

After the resol synthesis, the previously 3D-printed templates were filled with the resol, which was then left to cure at 353 K for one week. After curing, the templates (containing the cured resol) were immersed in a water bath at room temperature to dissolve the PVA template. The resol structures were subsequently dried at room temperature for one day and pyrolyzed under a N_2 atmosphere (aprox. 100 mL/min) at a heating rate of 5 K/min, up to 673 K (maintained for 1 h). Following this, the samples were further heated to a final temperature of 1073 K (at 5 K/min), which was held for 2 h, and then cooled to room temperature

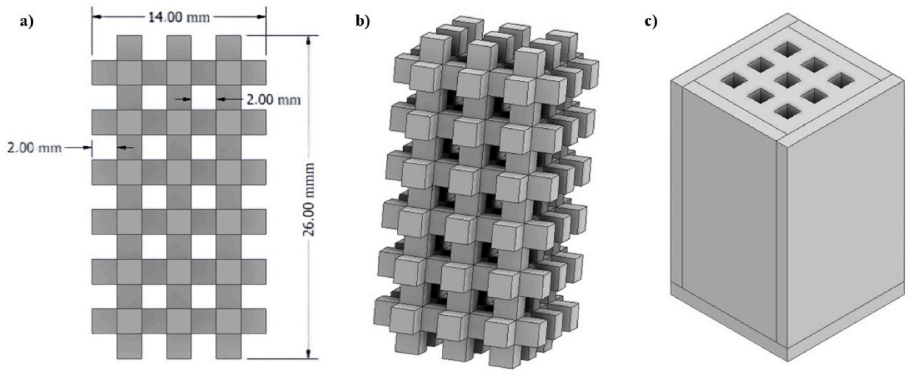

Fig. 1. 3D Designed structures - (a) Dimensions of the desired AC structure; (b) Front view of the structure; (c) Template for the structure to be 3D printed.

under N_2 flow.

The physical activation to increase porosity was performed by CO_2 activation. The resulting char structures were heated under a N_2 atmosphere at a constant heating rate of 5 K/min up to 1073 K. At this temperature, the N_2 atmosphere was replaced with CO_2 to carry out the activation process. The CO_2 atmosphere at 1073 K was maintained for specific periods (1, 2, or 3 h, depending on the sample), after which the system was cooled to room temperature under a N_2 atmosphere. The samples activated under CO_2 flow for 1, 2, and 3 h were labeled as AC_1, AC_2, and AC_3, respectively.

2.4. Characterization of the activated carbons

N_2 adsorption isotherms at 77 K were measured using an Autosorb IQ series equipment (Quantachrome). Prior to analysis, the samples were degassed under vacuum at 383 K for 3 h to remove any adsorbed species (e.g., moisture or other contaminants), ensuring accurate measurements. Thermogravimetric analysis (TGA) confirmed that the material is thermally stable at the selected degassing temperature, preventing structural degradation or changes in porosity. Possible operational error sources, such as gas contamination or system leaks, were carefully checked to ensure the reliability of the data. The surface area (A_{BET}) was determined using the Brunauer–Emmett–Teller (BET) method, while the total pore volume (v_p) was calculated at a relative pressure of $P/P_0 = 0.95$, assuming that the pores were filled with condensed liquid N_2 at its normal boiling point. The micropore volume was estimated using the *t*-plot method and the pore size distribution for micro- and mesoporosity was evaluated using Density Functional Theory (DFT).

Mercury Intrusion Porosimetry was conducted using an Autopore IV 9500 Instrument (Micromeritics, USA). The measurements were performed at pressures up to 30,000 psia with an equilibrium time of 20 s. Prior to mercury intrusion, the samples were degassed using the same procedure as for N_2 adsorption at 77 K.

Scanning Electron Microscopy (SEM) was performed on a Phenom SEM workstation (ThermoFisher) with an acceleration voltage of 10 kV. SEM was used to examine the surface morphology and microstructure of the ACs.

Thermogravimetric Analysis (TGA) was carried out using a Labsys Evo DTA/DSC system from SETARAM Instrumentation under an argon flow rate of 50 mL/min, with a mass sample around 10 mg. The TGA was performed by heating the samples at a 5 K/min rate, from 303 K up to a maximum temperature of 1173 K.

Differential Scanning Calorimetry (DSC) was conducted on a DSC Q2000 from TA Instruments Inc. (Tzero DSC Technology), coupled to an RCS 90 refrigeration system and operating in the "Heat Flow T4P″ mode. Measurements were performed under anhydrous conditions, purged with a high-purity N_2 flow rate of 50 mL/min. The instrument calibration was performed over a temperature range of 183–523 K. For each experiment, 7–12 mg of sample were weighed and encapsulated in a Tzero hermetic aluminum pan with a lid. Each pan was sealed before analysis, and the lid was perforated to prevent pressure build-up due to water evaporation. The experimental procedure consisted of first equilibrating all samples at 293 K, followed by cooling to 183 K (10 K/min) and heating to 473 K (10 K/min). Both cooling and heating runs was repeated three times, ending the thermal study at the initial temperature of 293 K.

A procedure with three thermal cycles was employed to thermally characterize the materials. The first cycle was performed to remove volatile substances present in the sample, such as water or other residual solvents. The second cycle was then employed to study the thermal behavior of the dried compound, while the last cycle served to validate the results obtained in the second cycle. The final temperature of 473 K was selected based on the TGA results, which showed no signs of degradation up to this temperature. The DSC allowed the heat capacity of the prepared ACs to be determined.

2.5. Adsorption equilibrium measurements

Pure-component adsorption equilibrium isotherms for CO_2 and N_2 were measured at 303 K and up to 8 bar for all the prepared structured ACs. Prior to the experiments, the samples were degassed *in situ* under vacuum at 373 K for 3 h to remove any pre-adsorbed species. These measurements were performed using a standard static gravimetric method. Mass and pressure variations were monitored until equilibrium was reached in the measurement cell, i.e., until both quantities remain constant.

The experimental setup employed consisted of an ISOSORP 2000 high-pressure magnetic suspension balance (Rubotherm GmbH, Germany) with a resolution of 10^{-5} g, an uncertainty of $\leq$0.002 %, and a reproducibility of $\leq 3 \times 10^{-5}$ g for a maximum load of 25 g. The temperature was measured with a four-wire Pt100 probe (RS Amidata, Spain) and controlled to within 0.1 K of the setpoint value using an F32 HL thermostatic bath (Julabo GmbH, Germany). The pressure was determined with two transducers to ensure high measurement accuracy across all pressures: a Baratron model 627D (MKS Instruments GmbH, Germany) for 0–1 bar, with an accuracy of 0.12 % of the measured value, and a PX01C1-500A5T from Omegadyne Inc. (Sunbury, OH, USA) for 0–35 bar (accuracy of 0.05 % FS). The pressure and sample weight were monitored and recorded online using in-house developed software. A schematic representation of the apparatus is shown in Fig. S.I.1 (Supporting Information). Detailed information of the experimental apparatus and methodology can be found elsewhere [22,36–38].

3. Theoretical

3.1. Single-component adsorption equilibrium

Several approaches can be utilized to report adsorption equilibrium

measurements, such as expressing the data as excess amount adsorbed, q_{ex}, which is calculated as

$$q_{ex} = \frac{w - m_s - m_h + V_h\rho_g}{m_s} + v_s\rho_g \quad (1)$$

where w is the mass measured in the balance; m_s is the mass of the AC; V_h and m_h are the volume and mass of the measuring cell, respectively, that contribute to buoyancy effects; ρ_g is the gas density at the experimental equilibrium pressure and temperature, which, in this work, was obtained using data from the National Institute of Standards and Technology (NIST) Chemistry Webbook [39]; and v_s (where $v_s = 1/\rho_s$, with ρ_s being the skeletal density of the solid matrix) is the specific volume of the solid matrix. Herein, v_s was determined from the data obtained through helium pycnometry performed at 303 K in the gravimetric apparatus, assuming negligible He adsorption.

Excess adsorption, q_{ex}, can be converted to absolute amount adsorbed, q, by

$$q = q_{ex}\left(\frac{\rho_l}{\rho_l - \rho_g}\right) \quad (2)$$

where it is assumed that the adsorbed phase density is equivalent to the liquid density at its boiling point under 1 atm (ρ_l) [40].

3.2. Toth isotherm model

The experimental single-component adsorption equilibrium data for CO_2 and N_2 were fitted using the semi-empirical Toth isotherm model, which is expressed as follows [41]:

$$q = \frac{q_s bP}{\left[1 + (bP)^t\right]^{1/t}} \quad (3)$$

where q represents the equilibrium concentration of the adsorbed phase (amount of adsorbate per unit mass of solid), q_s is the maximum adsorbed amount, b is the adsorption affinity constant, and t is the Toth constant, characteristic of the surface heterogeneity of the solid. The system is more heterogeneous as the t parameter deviates further from unity. On the other hand, the Toth model simplifies to the Langmuir isotherm model when $t = 1$.

3.3. Binary adsorption equilibrium prediction: Ideal adsorbed solution theory

The Ideal Adsorbed Solution Theory (IAST), originally developed by Myers and Prausnitz, is a thermodynamically consistent approach widely used to predict multicomponent adsorption equilibria based on pure component adsorption isotherm data [42]. One of its key advantages is its flexibility in predicting multicomponent adsorption without being tied to a specific pure component isotherm model. However, the accuracy of IAST predictions depends not only on the system under study but also on the quality of the pure component data fitting. Specifically, significant errors —particularly in the low-pressure region — can affect the multicomponent adsorption results [41].

In this study, the IAST was employed in conjunction with the Toth adsorption isotherm model. While IAST is effective for describing multicomponent equilibrium in multicolumn adsorption processes (e.g., pressure swing adsorption), it can be computationally intensive due to the iterative nature of solving the defining equations. Consequently, analytical formulations are often preferred for process simulations [43]. An example of such an analytical approach is the multicomponent extension of the Toth model, which is expressed as

$$q_i = \frac{q_{i,s} b_i p_i}{\left[1 + \left(\sum_j b_j p_j\right)^{t_i}\right]^{1/t_i}} \quad (4)$$

Given that the goal of this work is to develop structured materials for CO_2 capture from post-combustion flue gases, it is crucial for the material to exhibit selective adsorption capacity for CO_2 over N_2. The selectivity in a binary mixture is commonly determined using the following expression:

$$\alpha_{CO_2/N_2} = \frac{q_{CO_2}/q_{N_2}}{y_{CO_2}/y_{N_2}} \quad (5)$$

where α_{CO_2/N_2} is the CO_2/N_2 selectivity, y_i is the mole fraction of component i in the mixture and q_i is its amount adsorbed. The selectivity was calculated for a binary mixture with a CO_2 mole fraction of 15 %, typical of flue gases derived from coal-fired power plants.

4. Results and discussion

4.1. Characterization of the activated carbons

4.1.1. N_2 adsorption at 77 K

The N_2 sorption isotherms at 77 K were measured for the 3D activated carbon structures. The data obtained are presented in Fig. 2, and the specific surface area (A_{BET}), total pore volume (v_P), micropore volume (v_{micro}) and burn-off percentage are summarized in Table 1.

The ACs exhibit a type Ib isotherm with a H4 hysteresis loop, characteristic of microporous activated carbons containing some mesoporosity [44]. It was observed that increasing the activation time (i.e., a longer period under CO_2 flow) resulted in a higher burn-off (Table 1), which represents the percentage of carbon removed during the activation process due to gasification reactions with CO_2. A higher burn-off leads to a rise in surface area, pore volume, and micropore volume as more carbon is etched away, creating and expanding porosity within the material. The shape of the isotherms changes slightly with the CO_2 activation time of the material. AC_1 presents an isotherm with a plateau-like region, while AC_2 and AC_3 isotherms display a more pronounced isotherm loop and a gradual rise in the amount of N_2 adsorbed with the relative pressure, indicating the expansion of pore volume. This is in line with previous studies on the preparation of activated carbons from phenolic resins, where prolonged CO_2 activation has been shown to increase surface area and pore volume, as well as expand microporosity [45,46]. During CO_2 activation at 1073 K, carbon materials react with CO_2, resulting in the selective etching of carbon atoms and the formation of vacancies and defects. Normally, the basal planes of graphitic carbon are more resistant to CO_2 activation, while the amorphous or defect-rich regions suffer a faster attack [47,48]. This explains the need for a longer

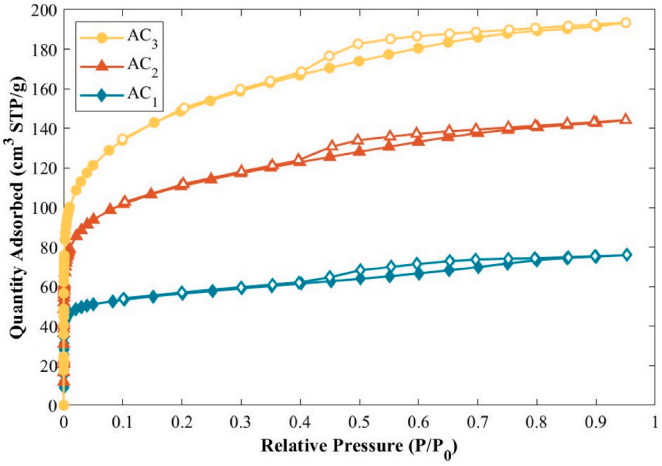

Fig. 2. N_2 adsorption-desorption isotherms at 77 K of activated carbon 3D structures AC_1 (◆), AC_2 (▲), and AC_3 (●). Filled and empty symbols denote adsorption and desorption data, respectively.

Table 1
Textural properties of the 3D printed activated carbons.

Sample	Burn-off (%)	N_2 Adsorption data at 77 K			Hg Intrusion data		
		A_{BET} (m^2/g)	v_P (cm^3/g)	v_{micro} (cm^3/g)	Skeletal Density (g/mL)	Average Pore Diameter (μm)	Porosity (%)
AC_1	19	214	0.12	0.08	1.19	26.1	18
AC_2	36	407	0.22	0.19	1.27	26.7	19
AC_3	49	539	0.30	0.26	1.33	70.3	37

exposure to CO_2 (at least 2 h) to achieve a well-developed porosity, as seen in AC_2. Such extended activation time enhances both the specific surface area and overall porosity of the material. As activation progresses, the continuous removal of carbon atoms leads to pore expansion and the merging of adjacent micropores into mesopores, justifying the increase in average pore size observed in AC_3 after 3 h of CO_2 activation. Nonetheless, excessive carbon removal can thin the pore walls, compromising mechanical stability and potentially causing the monolith's macrostructure to collapse. To avoid this, the maximum activation time was limited to 3 h.

Fig. 3 shows the pore size distribution (PSD) of the ACs studied, indicating a broad micropore distribution across the entire microporosity range, with some narrow mesopores also present. This pattern is in agreement with the N_2 adsorption isotherm at 77 K type, as type Ib isotherms are characteristic of materials with wide micropores and narrow mesopores [44]. The primary contribution to pore volume comes from pores in the range of approximately 5 Å to 10 Å. However, a significant proportion of narrow micropores, smaller than ~4 Å, is also observed.

4.1.2. Mercury porosimetry

Mercury Intrusion Porosimetry was performed to characterize the macroporous structure of the 3D AC monoliths. Fig. 4 shows the resulting PSD, while Table 1 lists the skeletal density, average pore diameter, and porosity of each sample.

All ACs exhibit a non-uniform macropore distribution. The three samples display similar distributions, with larger macropore widths above ~1 μm, as well as smaller macropores and large mesopores within the range of 0.01–0.1 μm. Despite having porosity within similar ranges, AC_1 and AC_2 present very similar pore volumes, whereas AC_3 shows a much larger pore volume. This highlights the impact of a longer activation time on the overall porosity of the carbon material, resulting in an improved porosity of 37 %, compared to 18 % and 19 % for AC1 and AC2, respectively.

Nevertheless, it is worth noting that the macropore volume is lower in comparison to other ACs produced via 3D printing using DIW, as

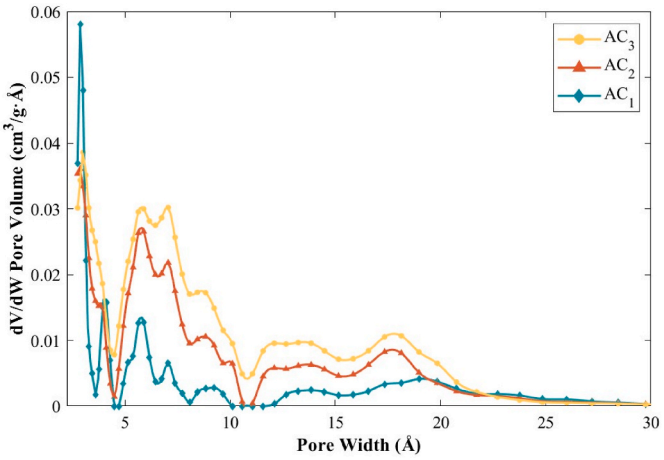

Fig. 3. Pore size distribution of AC_1, AC_2, and AC_3 determined by applying the Density Functional Theory (DFT) method to the N_2 isotherms at 77 K.

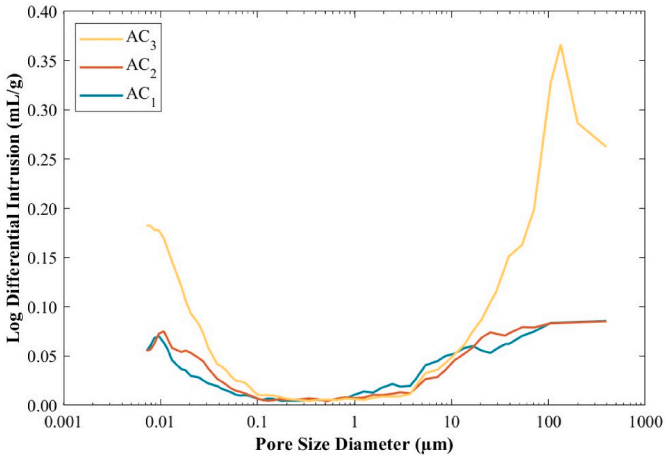

Fig. 4. Pore size distribution of AC_1, AC_2, and AC_3 determined by Hg porosimetry.

previously reported [24,26,27]. The skeletal density is similar across all AC samples, although a slight rise was observed with activation time, which may indicate the removal of a lower-density carbon fraction during the CO_2 activation process [49]. The average pore diameter is comparable for AC_1 and AC_2 but increases significantly in AC_3, suggesting that the activation process progressively promotes the formation of larger pores, which could be advantageous for enhanced CO_2 transport.

4.1.3. Scanning Electron Microscopy (SEM)

The analysis of the SEM images demonstrates that the AC structures exhibit non-homogeneous surfaces (Fig. 5), revealing a non-uniform, broad macropore size distribution (Fig. 5b–d, f). The 3D AC structures have a reduced wall thickness compared to the 3D geometric model designed, which had a wall thickness of 2 mm. The obtained ACs exhibit thinner wall thicknesses: AC_3 (1.27 mm, Fig. 5e) < AC_2 (1.38 mm, Fig. 5c) < AC_1 (1.5 mm, Fig. 5a). This trend of decreasing wall thickness correlates with activation time, indicating that AC_3, subjected to the longest activation with CO_2, experienced the most significant reduction in wall thickness due to the partial gasification of the material.

Additionally, material contraction during the resol curing phase within the template, likely contributes to the reduction in wall thickness. This contraction results from the chemical volume loss during the polymerization reaction, followed by thermal contraction during cooling after curing [50]. Moreover, shrinkage affects not only the channel walls but also the channel size, suggesting that the entire structure undergoes uniform contraction. This decrease in both wall thickness and channel size may impact the structural integrity and mechanical properties of the 3D AC structures. Thus, longer activation times may lead to thinner walls and with potentially weaker structural and mechanical resistance.

The SEM analysis reveals the presence of crystals on the surface of the materials, with AC_1 shown as an example in Fig. 6. Energy Dispersive Spectroscopy (EDS) results (Fig. 7) identified the crystal elements as sodium (Na) and chlorine (Cl). These elements are attributed to the formation of sodium chloride (NaCl) as a byproduct of the acid-base

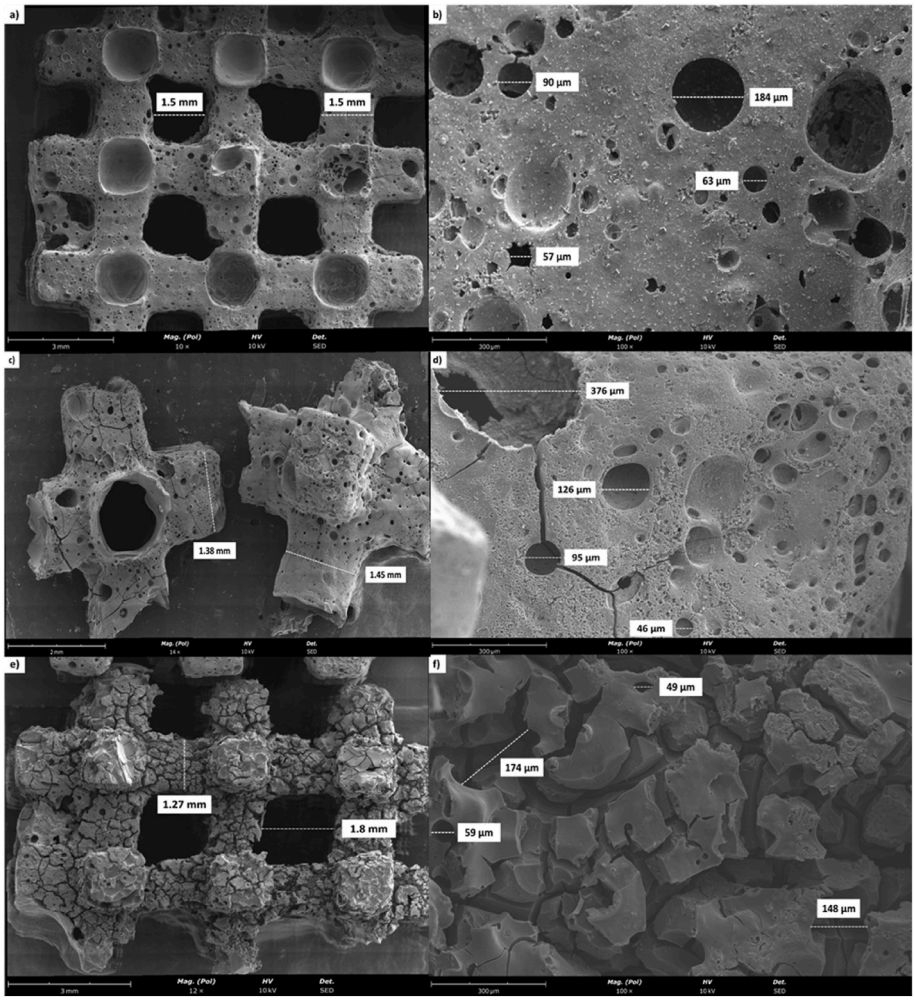

Fig. 5. SEM images of the activated carbon 3D structures: AC_1 at magnifications of (a) 10× and (b) 100x; AC_2 at magnifications of (c) 14× and (d) 100x; AC_3 at magnifications of (e) 12× and (f) 100x.

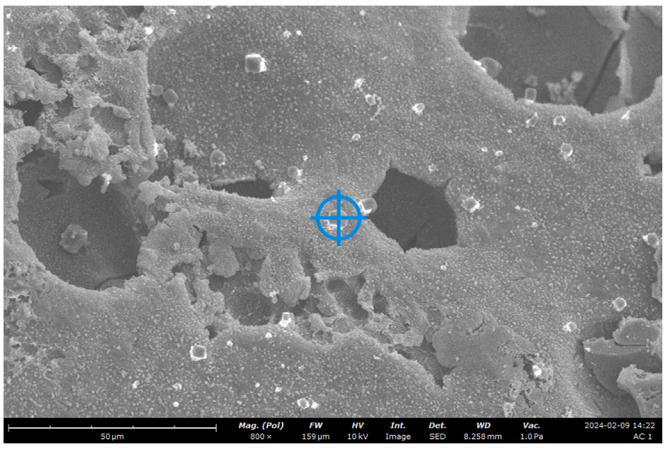

Fig. 6. SEM images of the activated carbon 3D structure AC_1 at magnifications of 800×.

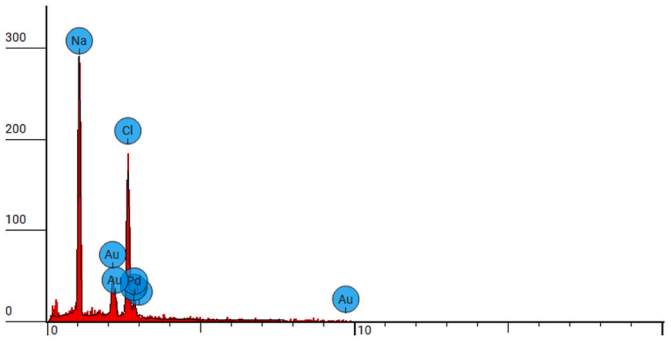

Fig. 7. EDS spectrum of the activated carbon 3D structure AC_1 at magnifications of 800×.

reaction carried out during the resol synthesis, where NaOH, used as a catalyst, was neutralized with HCl.

4.1.4. Thermogravimetric Analysis (TGA)

TGA was performed up to 1173 K to evaluate the thermal stability of the 3D AC structures. The TGA results (Fig. 8) indicate that all ACs show similar behavior with increasing temperature, undergoing degradation within the studied temperature range. The ACs are thermally stable up to approximately 673 K, showing minimal mass loss (~3 %), which can be attributed to the removal of adsorbed moisture and possibly other impurities. Beyond this point, a significant mass loss occurs, reaching approximately 40–50 % by the maximum temperature of 1173 K. Based on the TGA data, 373 K was selected as a suitable degassing temperature for the ACs prior to the adsorption equilibrium measurements.

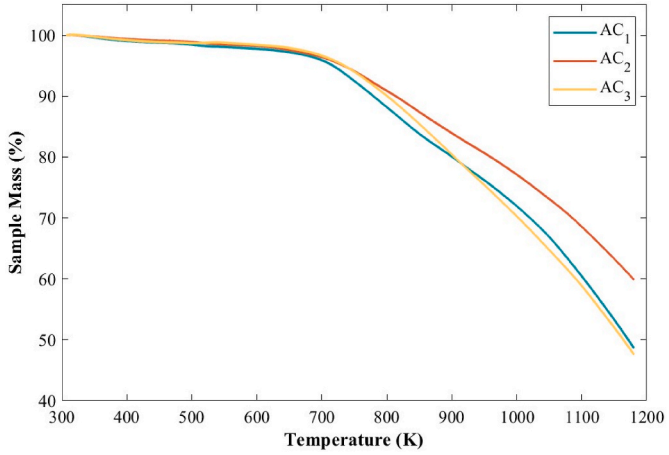

Fig. 8. Sample mass as a function of temperature obtained from TGA for the activated carbon 3D structures.

4.1.5. *Differential Scanning Calorimetry (DSC)*

The DSC thermograms of the ACs, plotted as a function of heat flow, are shown in Fig. S.I.2. These thermograms reveal no significant thermal events, except for the evaporation of water during the first heating run, which manifests as a broad endothermic peak in the heat flow. The specific heat capacity (C_p) of the ACs up to 473 K was calculated from the DSC data and is presented in Fig. 9. The C_p values exhibit a linear dependence on temperature, consistent with previous measurements for ACs derived from phenolic resin precursors [51], although the ACs in this study show slightly higher values.

The three AC samples have similar C_p values at room temperature, followed by the aforementioned linear increase. However, no clear relationship is observed between the heat capacities and the activation times (under CO_2 flow). Understanding the temperature dependence of C_p is important for accurately modelling temperature swing adsorption processes for CO_2 capture.

4.2. *Adsorption equilibria of CO_2 and N_2*

The adsorption equilibria of CO_2 and N_2 on the AC structures were measured at 303 K and pressures up to 8 bar. As shown in Fig. 10, the measured isotherms indicate that all materials exhibit favorable CO_2 adsorption behavior. The CO_2 adsorption capacities of AC_1, AC_2, and AC_3 are 3.16, 3.47, and 4.13 mol/kg, respectively, at the maximum studied pressure of 8 bar. These adsorption capacities correlate directly

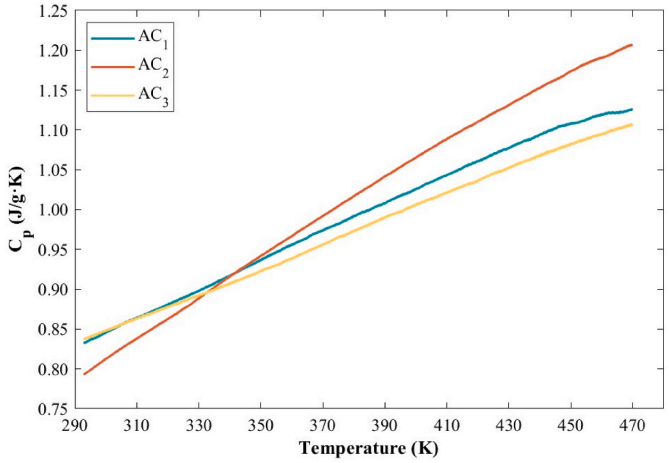

Fig. 9. Specific heat capacity of the 3D printed ACs as a function of temperature.

with the textural characteristics of the ACs. The observed trend in CO_2 adsorption capacities — $AC_1 < AC_2 < AC_3$ — is consistent with the specific surface area and micropore volume of the materials, as detailed in Table 1.

All ACs exhibited significantly lower N_2 adsorption capacity compared to CO_2. The adsorption capacities at 8 bar for AC_1, AC_2, and AC_3 are 0.42, 0.48, and 0.73 mol/kg, respectively. Once again, the adsorption capacities are consistent with the surface area and micropore volume of the samples (Table 1).

Among the three ACs, AC_3, which underwent the longest activation period, displays the most favorable textural properties (A_{BET}, v_p, and v_{micro}), as well as the highest adsorption capacities for both CO_2 and N_2. The prolonged exposure to the activation agent (CO_2) during the activation process results in a higher degree of carbon burn-off, leading to an increase in microporosity and, consequently, in surface area. This increase in porosity directly enhances the adsorption capacity at higher pressures, as a greater number of available adsorption sites facilitates gas uptake.

The CO_2 and N_2 adsorption equilibrium isotherms were fitted using the Toth model. The solid lines in Fig. 10 represent the Toth fit to the experimental adsorption data, demonstrating that this model accurately describes the data. The Toth model was selected because it provides a more flexible approach for describing heterogeneous adsorption systems compared to traditional models such as Langmuir or Freundlich. The Toth isotherm model parameters were determined by minimizing the sum of squared absolute errors between the calculated and experimental values. Additionally, the coefficient of determination (R^2) was calculated to further assess the quality of the fit, with values close to unity, confirming the accuracy of the model. The parameter values obtained are presented in Table 2.

Fig. 11 illustrates the selectivity predicted through the IAST model for a binary mixture with a molar composition of 15 % CO_2 ($y_{CO2} = 0.15$; $y_{N2} = 0.85$). Despite AC_1 exhibiting a lower CO_2 adsorption capacity compared to the other samples, it demonstrates the highest selectivity across the entire pressure range studied. This highlights the importance of a lower N_2 adsorption capacity in achieving higher CO_2 selectivity. This behavior of AC_1, i.e., the AC with shortest activation period showing higher CO_2/N_2 selectivity, is consistent with observations reported in the literature [33,52].

Although AC_1 has a smaller pore volume, it contains a significant amount of smaller micropores, which promote CO_2 adsorption in the low-pressure region (Fig. 10a). Its narrow micropore sizes allow for maximized CO_2 molecule-to-adsorbent wall interactions. This shows that the pore size distribution plays a crucial role in dictating the adsorption performance and that an optimal balance between pore volume and pore sizes is needed to optimize the adsorption properties of materials.

Therefore, a balance between selectivity and loading capacity must always be evaluated when choosing the adsorbent material with the best potential for any specific application.

5. Conclusions

In this work, AC monolithic structures with interconnected channels were successfully fabricated using the FDM technique to print sacrificial water-soluble templates, which were then employed to shape carbon structures derived from a phenolic resin. The preparation of the ACs evaluated the effect of activation time under CO_2 flow.

Characterization techniques provided detailed insights into the textural and thermal properties of the structured ACs. N_2 adsorption at 77 K indicates that longer activation times (under CO_2 flow) lead to a significant rise in surface area and pore volume, suggesting improved textural properties. This effect is associated with a higher burn-off level, as prolonged exposure to CO_2 enhances the gasification of carbon, promoting the development and expansion of porosity. Mercury Intrusion Porosimetry also reveals an improvement in porosity with

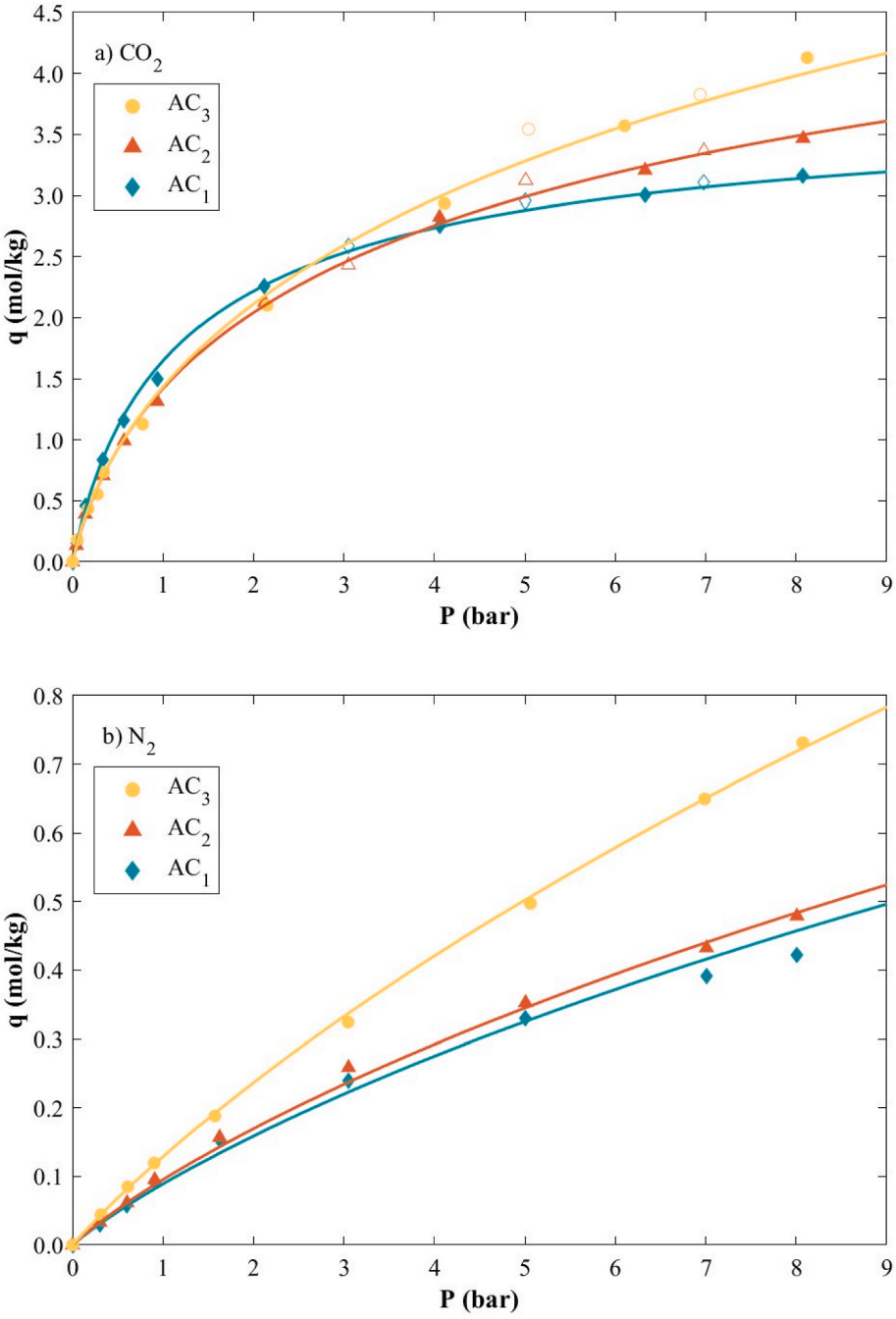

Fig. 10. Adsorption equilibrium of a) CO_2 and b) N_2 on the activated carbon 3D structures at 303 K. Filled and empty symbols denote adsorption and desorption experimental data, respectively; solid lines represent the Toth adsorption isotherm model.

Table 2
Toth model fitting parameters for CO_2 and N_2 single component adsorption equilibrium isotherms.

Sample	q_s (mol/kg)	b (bar^{-1})	t	Error (%)	R^2
		CO_2			
AC_1	3.86	1.00	0.81	0.02	0.999
AC_2	6.66	0.59	0.55	0.02	0.999
AC_3	13.50	0.38	0.40	0.04	0.996
		N_2			
AC_1	6.96	0.0180	0.45	0.06	0.988
AC_2	6.96	0.0196	0.45	0.04	0.997
AC_3	8.54	0.0185	0.54	0.02	0.999

activation time, consistent with the progressive gasification observed. SEM images show shrinkage of the monolithic walls compared to the designed structures, with this effect being more pronounced as the activation increases. SEM also allows for the observation of the macropore size distribution. On the other hand, thermal characterization shows that the ACs are thermally stable up to 673 K, with specific heat capacities ranging from 0.8 to 1.2 J/g·K in the temperature range of 293–473 K, making them suitable materials for TSA processes.

All ACs exhibit higher CO_2 adsorption capacities than N_2. The ACs activated for longer periods show higher CO_2 adsorption at higher pressures. However, the sample with the shortest activation time (AC_1) displays greater selectivity towards CO_2, when considering a CO_2 molar fraction of 0.15, primarily due to its lower N_2 adsorption capacity. Furthermore, this sample adsorbs more CO_2 than AC_2 and AC_3 in the

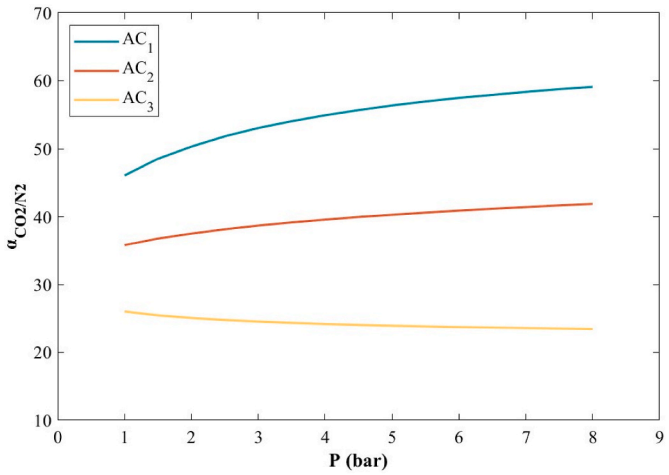

Fig. 11. CO_2/N_2 selectivity at 303 K for a mixture with 15 mol% of CO_2.

low-pressure region as a result of a significant portion of smaller micropores. The Toth isotherm model successfully fits the experimental equilibrium adsorption data for both CO_2 and N_2.

In conclusion, the 3D AC structures presented in this work are promising candidates for use as adsorbents in CO_2/N_2 mixture separation. The methodology applied for their preparation offers a straightforward approach to obtain optimized 3D structures, opening doors to develop optimized adsorbents. To implement these materials at an industrial level, it should be noted that further studies need be conducted to evaluate the feasibility of scaling-up the production of the 3D AC structures and the material stability upon multiple adsorption-desorption cycles.

CRediT authorship contribution statement

Henrry Ortega-Ortiz: Writing – original draft, Visualization, Methodology, Investigation, Formal analysis. **Laura M. Esteves:** Writing – review & editing, Investigation, Formal analysis, Conceptualization. **Andreia F.M. Santos:** Writing – review & editing, Investigation, Formal analysis. **Jeniffer Carrillo:** Writing – review & editing, Supervision. **Isabel M. Fonseca:** Writing – review & editing. **José P.B. Mota:** Writing – review & editing. **Inês Matos:** Writing – review & editing, Supervision, Methodology, Conceptualization. **Rui P.P.L. Ribeiro:** Writing – review & editing, Supervision, Resources, Funding acquisition, Formal analysis, Conceptualization.

Declaration of competing interest

The authors declare that they have no known competing financial interests or personal relationships that could have appeared to influence the work reported in this paper.

Acknowledgements

The authors acknowledge financial support from FCT/MCTES (Portugal) through project 2022.15637.UTA (Print3d4Capture) funded through the UT Austin-Portugal Program. This work was also partially supported by FCT/MCTES (Portugal) through Associate Laboratory for Green Chemistry–LAQV (LA/P/0008/2020, UIDP/50006/2020, UIDB/50006/2020). Inês Matos acknowledges the Individual Call to Scientific Employment Stimulus contract CEECIND 004431/2022. Andreia F. M. Santos acknowledges for funding under the PRR project InsectERA (nº C644917393-00000032). The authors would like to extend their appreciation to Daniela A. S. Agostinho (NOVA FCT) for her valuable support throughout this work.

Appendix A. Supplementary data

Supplementary data to this article can be found online at https://doi.org/10.1016/j.micromeso.2025.113621.

Data availability

Data will be made available on request.

References

[1] United States Enviromental Protection Agency (EPA), Overview of greenhouse gases. https://www.epa.gov/ghgemissions/overview-greenhouse-gases#carbon-dioxide, 2024. (Accessed 24 August 2024).
[2] A. Allangawi, E.F.H. Alzaimoor, H.H. Shanaah, H.A. Mohammed, H. Saqer, A.A. El-Fattah, A.H. Kamel, Carbon capture materials in post-combustion: adsorption and Absorption-based processes, C (Basel) 9 (2023) 17, https://doi.org/10.3390/c9010017.
[3] S. Vaz, A.P. Rodrigues de Souza, B.E. Lobo Baeta, Technologies for carbon dioxide capture: a review applied to energy sectors, Clean Eng Technol 8 (2022) 100456, https://doi.org/10.1016/j.clet.2022.100456.
[4] J.F.D. Tapia, J.-Y. Lee, R.E.H. Ooi, D.C.Y. Foo, R.R. Tan, A review of optimization and decision-making models for the planning of CO2 capture, utilization and storage (CCUS) systems, Sustain. Prod. Consum. 13 (2018) 1–15, https://doi.org/10.1016/j.spc.2017.10.001.
[5] B.C.R. Camacho, R.P.P.L. Ribeiro, I.A.A.C. Esteves, J.P.B. Mota, Adsorption equilibrium of carbon dioxide and nitrogen on the MIL-53(Al) metal organic framework, Sep. Purif. Technol. 141 (2015) 150–159, https://doi.org/10.1016/j.seppur.2014.11.040.
[6] J. van Heek, K. Arning, M. Ziefle, Reduce, reuse, recycle: acceptance of CO2-utilization for plastic products, Energy Policy 105 (2017) 53–66, https://doi.org/10.1016/j.enpol.2017.02.016.
[7] F. Raganati, F. Miccio, P. Ammendola, Adsorption of carbon dioxide for post-combustion capture: a review, Energy & Fuels 35 (2021) 12845–12868, https://doi.org/10.1021/acs.energyfuels.1c01618.
[8] S. Kumar, R. Srivastava, J. Koh, Utilization of zeolites as CO2 capturing agents: advances and future perspectives, J. CO2 Util. 41 (2020) 101251, https://doi.org/10.1016/j.jcou.2020.101251.
[9] F. Brandani, D.M. Ruthven, The effect of water on the adsorption of CO2 and C3H8 on type X zeolites, Ind. Eng. Chem. Res. 43 (2004) 8339–8344, https://doi.org/10.1021/ie040183o.
[10] R. Kodasma, J. Fermoso, A. Sanna, Li-LSX-zeolite evaluation for post-combustion CO2 capture, Chem. Eng. J. 358 (2019) 1351–1362, https://doi.org/10.1016/j.cej.2018.10.063.
[11] T. Ghanbari, F. Abnisa, W.M.A. Wan Daud, A review on production of metal organic frameworks (MOF) for CO2 adsorption, Sci. Total Environ. 707 (2020) 135090, https://doi.org/10.1016/j.scitotenv.2019.135090.
[12] Z. Yuan, M.R. Eden, R. Gani, Toward the development and deployment of large-scale carbon dioxide capture and conversion processes, Ind. Eng. Chem. Res. 55 (2016) 3383–3419, https://doi.org/10.1021/acs.iecr.5b03277.
[13] M. Younas, M. Rezakazemi, M. Daud, M.B. Wazir, S. Ahmad, N. Ullah, Inamuddin, S. Ramakrishna, Recent progress and remaining challenges in post-combustion CO2 capture using metal-organic frameworks (MOFs), Prog. Energy Combust. Sci. 80 (2020) 100849, https://doi.org/10.1016/j.pecs.2020.100849.
[14] U. Kamran, S.-J. Park, Chemically modified carbonaceous adsorbents for enhanced CO2 capture: a review, J. Clean. Prod. 290 (2021) 125776, https://doi.org/10.1016/j.jclepro.2020.125776.
[15] J. Yang, L. Yue, X. Hu, L. Wang, Y. Zhao, Y. Lin, Y. Sun, H. DaCosta, L. Guo, Efficient CO2 capture by porous carbons derived from coconut shell, Energy & Fuels 31 (2017) 4287–4293, https://doi.org/10.1021/acs.energyfuels.7b00633.
[16] D.Y.C. Leung, G. Caramanna, M.M. Maroto-Valer, An overview of current status of carbon dioxide capture and storage technologies, Renew. Sustain. Energy Rev. 39 (2014) 426–443, https://doi.org/10.1016/j.rser.2014.07.093.
[17] A. Modak, S. Jana, Advancement in porous adsorbents for post-combustion CO2 capture, Microporous Mesoporous Mater. 276 (2019) 107–132, https://doi.org/10.1016/j.micromeso.2018.09.018.
[18] A.M. Varghese, G.N. Karanikolos, CO2 capture adsorbents functionalized by amine – bearing polymers: a review, Int. J. Greenh. Gas Control 96 (2020) 103005, https://doi.org/10.1016/j.ijggc.2020.103005.
[19] A.E. Creamer, B. Gao, Carbon-based adsorbents for postcombustion CO2 capture: a critical review, Environ. Sci. Technol. 50 (2016) 7276–7289, https://doi.org/10.1021/acs.est.6b00627.
[20] S. Choi, J.H. Drese, C.W. Jones, Adsorbent materials for carbon dioxide capture from large anthropogenic point sources, ChemSusChem 2 (2009) 796–854, https://doi.org/10.1002/cssc.200900036.
[21] A. Almeida, R.P.P.L. Ribeiro, J.P.B. Mota, C. Grande, Extrusion and characterization of high Si/Al ratio ZSM-5 using silica binder, Energies 13 (2020) 1201, https://doi.org/10.3390/en13051201.
[22] R.P.P.L. Ribeiro, C.L. Antunes, A.U. Garate, A.F. Portela, M.G. Plaza, J.P.B. Mota, I. A.A.C. Esteves, Binderless shaped metal-organic framework particles: impact on carbon dioxide adsorption, Microporous Mesoporous Mater. 275 (2019) 111–121, https://doi.org/10.1016/j.micromeso.2018.08.002.

[23] W.Y. Hong, S.P. Perera, A.D. Burrows, Manufacturing of metal-organic framework monoliths and their application in CO2 adsorption, Microporous Mesoporous Mater. 214 (2015) 149–155, https://doi.org/10.1016/j.micromeso.2015.05.014.
[24] D.N.D.L. Mendes, A. Gaspar, I. Ferreira, J.P.B. Mota, R.P.P.L. Ribeiro, 3D-printed hybrid zeolitic/carbonaceous electrically conductive adsorbent structures, Chem. Eng. Res. Des. 174 (2021) 442–453, https://doi.org/10.1016/j.cherd.2021.08.020.
[25] M.J. Regufe, A.F.P. Ferreira, J.M. Loureiro, A. Rodrigues, A.M. Ribeiro, Electrical conductive 3D-printed monolith adsorbent for CO2 capture, Microporous Mesoporous Mater. 278 (2019) 403–413, https://doi.org/10.1016/j.micromeso.2019.01.009.
[26] A. Pereira, A.F.P. Ferreira, A. Rodrigues, A.M. Ribeiro, M.J. Regufe, Study of methane upgrading using an activated carbon 3D-printed adsorbent, J. Environ. Chem. Eng. 12 (2024) 111730, https://doi.org/10.1016/j.jece.2023.111730.
[27] A. Pereira, A.F.P. Ferreira, A. Rodrigues, A.M. Ribeiro, M.J. Regufe, Evaluation of the potential of a 3D-printed hybrid zeolite 13X/activated carbon material for CO2/N2 separation using electric swing adsorption, Chem. Eng. J. 450 (2022) 138197, https://doi.org/10.1016/j.cej.2022.138197.
[28] H. Thakkar, S. Eastman, Q. Al-Naddaf, A.A. Rownaghi, F. Rezaei, 3D-Printed metal–organic framework monoliths for gas adsorption processes, ACS Appl. Mater. Interfaces 9 (2017) 35908–35916, https://doi.org/10.1021/acsami.7b11626.
[29] H. Thakkar, S. Eastman, A. Hajari, A.A. Rownaghi, J.C. Knox, F. Rezaei, 3D-Printed zeolite monoliths for CO2 removal from enclosed environments, ACS Appl. Mater. Interfaces 8 (2016) 27753–27761, https://doi.org/10.1021/acsami.6b09647.
[30] S. Couck, J. Lefevere, S. Mullens, L. Protasova, V. Meynen, G. Desmet, G.V. Baron, J.F.M. Denayer, CO2, CH4 and N2 separation with a 3DFD-printed ZSM-5 monolith, Chem. Eng. J. 308 (2017) 719–726, https://doi.org/10.1016/j.cej.2016.09.046.
[31] K.B. Jivrakh, A.M. Varghese, S. Ehrling, S. Kuppireddy, K. Polychronopoulou, R. K. Abu Al-Rub, N. Alamoodi, G.N. Karanikolos, 3D-printed zeolite 13X gyroid monolith adsorbents for CO2 capture, Chem. Eng. J. 497 (2024) 154674, https://doi.org/10.1016/j.cej.2024.154674.
[32] S. Lawson, M. Snarzyk, D. Hanify, A.A. Rownaghi, F. Rezaei, Development of 3D-printed polymer-MOF monoliths for CO2 adsorption, Ind. Eng. Chem. Res. 59 (2020) 7151–7160, https://doi.org/10.1021/acs.iecr.9b05445.
[33] L.F.A.S. Zafanelli, A. Henrique, H. Steldinger, J.L. Diaz de Tuesta, J. Gläsel, A. E. Rodrigues, H.T. Gomes, B.J.M. Etzold, J.A.C. Silva, 3D-printed activated carbon for post-combustion CO2 capture, Microporous Mesoporous Mater. 335 (2022) 111818, https://doi.org/10.1016/j.micromeso.2022.111818.
[34] A.J.A. Abubakar, R.L.S. Canevesi, D.A.L. Sanchez, C.A. Grande, Monoliths for gas storage manufactured with precision pore engineering using 3D-printed templates, Chem. Eng. J. 489 (2024) 151450, https://doi.org/10.1016/j.cej.2024.151450.
[35] Y. Meng, D. Gu, F. Zhang, Y. Shi, H. Yang, Z. Li, C. Yu, B. Tu, D. Zhao, Ordered mesoporous polymers and homologous carbon frameworks: amphiphilic surfactant templating and direct transformation, Angew. Chem. 117 (2005) 7215–7221, https://doi.org/10.1002/ange.200501561.
[36] R.P.P.L. Ribeiro, B.C.R. Camacho, A. Lyubchyk, I.A.A.C. Esteves, F.J.A.L. Cruz, J.P. B. Mota, Experimental and computational study of ethane and ethylene adsorption in the MIL-53(Al) metal organic framework, Microporous Mesoporous Mater. 230 (2016) 154–165, https://doi.org/10.1016/j.micromeso.2016.05.006.
[37] J.E. Sosa, C. Malheiro, R.P. Ribeiro, P.J. Castro, M.M. Piñeiro, J.M. Araújo, F. Plantier, J.P. Mota, A.B. Pereiro, Adsorption of fluorinated greenhouse gases on activated carbons: evaluation of their potential for gas separation, Journal of Chemical Technology & Biotechnology 95 (2020) 1892–1905, https://doi.org/10.1002/jctb.6371.
[38] J.E. Sosa, R.P.P.L. Ribeiro, I. Matos, M. Bernardo, I.M. Fonseca, J.P.B. Mota, J.M. M. Araújo, A.B. Pereiro, Exploring the potential of biomass-derived carbons for the separation of fluorinated gases with high global warming potential, Biomass Bioenergy 188 (2024) 107323, https://doi.org/10.1016/j.biombioe.2024.107323.
[39] National Institute of Standards and Technology (NIST) Chemistry WebBook, Thermophysical properties of fluid systems. https://webbook.nist.gov/chemistry/fluid/, 2024. (Accessed 31 January 2024).
[40] F. Dreisbach, R. Staudt, J.U. Keller, High pressure adsorption data of methane, nitrogen, carbon dioxide and their binary and ternary mixtures on activated carbon, Adsorption 5 (1999) 215–227, https://doi.org/10.1023/A:1008914703884.
[41] D.D. Do, Adsorption Analysis: Equilibria and Kinetics, Imperial College Press, 1998, https://doi.org/10.1142/9781860943829.
[42] A.L. Myers, Adsorption of gas mixtures-A thermodynamic approach, Ind. Eng. Chem. 60 (1968) 45–49, https://doi.org/10.1021/ie50701a007.
[43] M.A. Granato, V.D. Martins, J.C. Santos, M. Jorge, A.E. Rodrigues, From molecules to processes: molecular simulations applied to the design of simulated moving bed for ethane/ethylene separation, Can. J. Chem. Eng. 92 (2014) 148–155, https://doi.org/10.1002/cjce.21805.
[44] M. Thommes, Physisorption of gases, with special reference to the evaluation of surface area and pore size distribution (IUPAC Technical Report), Chem. Int. 38 (2016) 25, https://doi.org/10.1515/ci-2016-0119, 25.
[45] A. Singh, D. Lal, Microporous activated carbon spheres prepared from resole-type crosslinked phenolic beads by physical activation, J. Appl. Polym. Sci. 110 (2008) 3283–3291, https://doi.org/10.1002/app.28846.
[46] C.F. Martín, M.G. Plaza, S. García, J.J. Pis, F. Rubiera, C. Pevida, Microporous phenol–formaldehyde resin-based adsorbents for pre-combustion CO2 capture, Fuel 90 (2011) 2064–2072, https://doi.org/10.1016/j.fuel.2011.01.019.
[47] S.-M. Lee, S.-H. Lee, S.-H. Kim, J.-S. Roh, Analysis of pore formation and development in carbon blacks activated in a CO2 gas atmosphere through microstructural observation, Carbon Lett. 31 (2021) 1317–1326, https://doi.org/10.1007/s42823-021-00284-9.
[48] I. Yang, M. Jung, M.-S. Kim, D. Choi, J.C. Jung, Physical and chemical activation mechanisms of carbon materials based on the microdomain model, J Mater Chem A Mater 9 (2021) 9815–9825, https://doi.org/10.1039/D1TA00765C.
[49] S.R. Tennison, Phenolic-resin-derived activated carbons, Appl. Catal. Gen. 173 (1998) 289–311, https://doi.org/10.1016/S0926-860X(98)00186-0.
[50] S. Pansart, Prepreg processing of advanced fibre-reinforced polymer (FRP) composites, in: J. Bai (Ed.), Advanced Fibre-Reinforced Polymer (FRP) Composites for Structural Applications, Elsevier, 2013, pp. 125–154, https://doi.org/10.1533/9780857098641.2.125.
[51] N. Querejeta, S. García, N. Álvarez-Gutiérrez, F. Rubiera, C. Pevida, Measuring heat capacity of activated carbons for CO2 capture, J. CO2 Util. 33 (2019) 148–156, https://doi.org/10.1016/j.jcou.2019.05.018.
[52] N. Querejeta, M.G. Plaza, F. Rubiera, C. Pevida, T. Avery, S.R. Tennisson, Carbon monoliths in adsorption-based post-combustion CO2 capture, Energy Proc. 114 (2017) 2341–2352, https://doi.org/10.1016/j.egypro.2017.03.1366.